Nanoscale Advances

PAPER

View Article Online
View Journal | View Issue

Open Access Article. Published on 05 November 2019. Downloaded on 1/24/2026 9:40:33 AM.
This article is licensed under a Creative Commons Attribution-NonCommercial 3.0 Unported Licence.

Check for updates

Cite this: *Nanoscale Adv.*, 2019, **1**, 4870

High performance indium oxide nanoribbon FETs: mitigating devices signal variation from batch fabrication†

Thuy Thi Thanh Pham, Duy Phu Tran and Benjamin Thierry *

Received 19th September 2019
Accepted 4th November 2019

DOI: 10.1039/c9na00592g

rsc.li/nanoscale-advances

Nanostructured field effect transistor (FET) based sensors have emerged as a powerful bioanalytical technology. However, performance variations across multiple devices and between fabrication batches inevitably exist and present a significant challenge holding back the translation of this cutting-edge technology. We report an optimized and cost-effective fabrication process for high-performance indium oxide nanoribbon FET with a steep subthreshold swing of 80 mV per decade. Through systematic electrical characterizations of 57 indium oxide nanoribbon FETs from different batches, we demonstrate an optimal operation point within the subthreshold regime that mitigates the issue of device-to-device performance variation. A non-linear pH sensing of the fabricated indium oxide nanoribbon FETs is also presented.

Introduction

Nanostructured FET based sensors have attracted extensive attention in chemical and biological sensing because of their direct signal transduction, exquisite sensitivity, and point-of-care integration capability.[1–4] Preferred materials for nano FET sensors construction include silicon (Si),[5–8] oxide semiconductors,[9–12] III–V materials,[13–15] and carbon based materials.[16–18] While Si-based nanoFETs (*e.g.* nanowires and nanoribbons) have been studied extensively,[6,7,19–22] significant recent research has focussed on semiconducting metal oxides towards better device performance and more scalable fabrication.[9–12,23–26] Of the studied oxides, In_2O_3 displays excellent features for sensing applications. For instance, excellent sensing performance for nanoscale In_2O_3 based FET sensors has been demonstrated for different bio/chemical/gas sensing applications.[9–11,16,24,27] Importantly, economical fabrication processes are available for nanoscale In_2O_3 FETs in large scale regardless of their substrate types (hard[9,10] or flexible[28,29] substrates). This makes In_2O_3 FETs readily compatible with point-of-care and wearable applications that typically require cost effectiveness in addition to the sensor's performance. In addition, the availability of high quality, commercial In_2O_3 target and the fact that In_2O_3 does not require impurity doping and dielectric isolation significantly simplify the fabrication process as well as the quality control. Finally, In_2O_3 is a wide bandgap material (bandgap of 3.6 eV)[30,31] and its electrical properties are much less affected by ambient temperature changes and visible light compared to that of low bandgap materials.[30,32] Although this remains to be experimentally verified, this feature is advantageous for the devices' translational implementation as well as simplifying the development of readout units.

Despite the great promises of nanoFET sensing technology, substantial device-to-device performance variations are inevitable and represent a significant limiting factor towards large-scale manufacturing. In order to mitigate device-to-device signal variations, a few approaches have been explored, including using mathematical calibration,[33] and predicting structural defects using optical methods.[34,35] Yet to date there has been no systematic studies elucidating how device operation conditions affect device-to-device signal variation. To address this important translational question, we first developed an optimized and cost-effective batch fabrication of In_2O_3 nanoribbon (NR) FETs which yielded excellent device's performance and structural uniformity. Utilizing only conventional microfabrication techniques (*i.e.* sputtering, photolithography), a remarkably low subthreshold swing (SS) of 80 mV per decade has been achieved for the In_2O_3 NR FET devices. A stringent set of quality control criteria (thickness uniformity, thin film surface roughness, material purity, and structural dimension uniformity) has been established in order to enable the reproducible and high-yield fabrication of device with high uniformity and excellent performance. Building on this optimized fabrication process, we then systematically characterized and analysed electrical signals to determine the optimal operating condition and suppress device-to-device signal variation. Normalized drain currents (I/I_0) from 57 In_2O_3 NR FETs from

Future Industries Institute, ARC Centre of Excellence in Convergent Bio-Nano Science and Technology, University of South Australia, Mawson Lakes Campus, Mawson Lakes, South Australia 5095, Australia. E-mail: benjamin.thierry@unisa.edu.au

† Electronic supplementary information (ESI) available. See DOI: 10.1039/c9na00592g

 This journal is © The Royal Society of Chemistry 2019

Open Access Article. Published on 05 November 2019. Downloaded on 1/24/2026 9:40:33 AM.
This article is licensed under a Creative Commons Attribution-NonCommercial 3.0 Unported Licence.

three different batches showed that devices had consistently higher signal resolution when operated in the subthreshold regime compared to linear regime operation. Moreover, subthreshold operation significantly suppressed device-to-device signal variation by at least two folds. Finally, the sensing capability of the fabricated In_2O_3 NR FETs was demonstrated with non-linear pH sensing from pH 4.0 to 10.0. Altogether, this study demonstrates the benefits of operating In_2O_3 NR FET devices under their optimum operating conditions in order to maximize the performance across devices fabricated at the wafer-scale.

Experimental

Device fabrication

In_2O_3, Au and Cr sputtering targets (99.99% purity) were purchased from Plasmaterials, Inc (US). AZ5214E and SU8 3005 photoresists and developers were obtained from MicroChem (US). Si wafers with 300 nm of thermal SiO_2 were purchased from University Wafer (US).

Briefly, the In_2O_3 NR FET fabrication process is illustrated in Fig. 1. Starting with a 4-inch Si wafer substrate with 300 nm of thermal SiO_2 on top (Fig. 1a), the first image reversal photolithography process using AZ5214E photoresist (details are in ESI†) and the first photomask were applied to define the lateral dimensions (3.7 μm wide and 14 μm long) of In_2O_3 NRs. Next, In_2O_3 NR structures were realized by a lift-off process using radio frequency (RF) sputtering (Edwards TF500 sputter coater, UK) (Fig. 1b). Another lift-off step was used to pattern electrical contact lines, source, drain and on-chip integrated gate electrodes using stack of 15 nm Cr/100 nm Au (Fig. 1c). A final photolithography step with SU8 3005 photoresist was carried out to form a passivation layer while opening a 10 μm sensing window over the In_2O_3 NRs as well as at integrated gate electrode areas (Fig. 1d). The wafers were finally diced into individual chips (W × L: 28.0 × 8.9 mm). Each chip has 4 independent In_2O_3 NR FETs connected separately to their source-drain electrodes and integrated electrode. For handling purpose, a dual in-line package (DIP-24) has been used to package the chip (Fig. 1e). The entire measurements were performed within a customised Faraday box (W × L: 20 × 30 cm) connected with a semiconductor analyser Keysight 2902A (US).

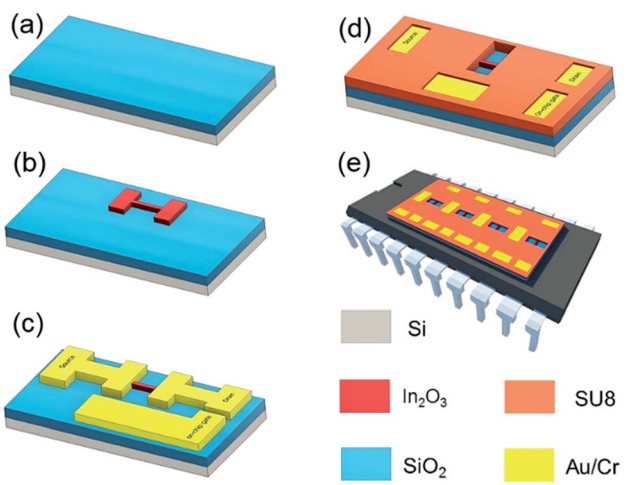

Fig. 1 Fabrication process of In_2O_3 NR FETs with on-chip integrated electrode. (a and b) Pattern of In_2O_3 nanostructure on the SiO_2/Si substrate after the first photolithography step, In_2O_3 deposition and lifting off; (c) define metallization feed lines, source, drain and on-chip integrated gate electrodes using Cr/Au lift-off; (d) device passivation with SU8 photoresist with open sensing area, integrated gate electrode and bonding pads; (e) packaging the In_2O_3 NR FET sensor into DIP 24 ceramic carrier.

Device characterizations

In_2O_3 NRs thickness and surface roughness were measured using atomic force microscopy (AFM, Veeco Multimode 8 microscope). Wafer-scale thickness mapping of the sputtered In_2O_3 thin film was carried out using ellipsometry (J. A. Woollam, US). Scanning electron microscopy (SEM) imaging of the In_2O_3 nanoribbons was conducted with a GEMINI II SEM (Zeiss, Germany). Percentages of indium in the sputtered In_2O_3 thin film were measured using a Kratos X-ray photoelectron spectroscopy (XPS, Japan). Gate bias was applied from the liquid front gate *via* on-chip integrated Au electrodes immersed in phosphate buffer saline (1× PBS, pH 7.4, electrical conductivity 15.5 mS cm^{-1}). In_2O_3 NR FETs were first washed thoroughly with acetone, propanol-2, deionized water, dried under N_2 gas and treated with UV-ozone for 1 hours to remove any residual contaminants prior characterizations.

After cleaning, pH measurements were carried out on unfunctionalized In_2O_3 NR FETs. The sensors were exposed to a solution of specific pH and allowed 5 min to establish equilibrium. The transfer curves for the devices were obtained from subthreshold to max g_m and over to saturation regions by scanning V_{GS} from 0–1.5 V. The devices were washed thoroughly with deionized water and dried with a N_2 stream prior to each measurement. We extracted drain current, I_{DS}, from the transfer curves at $V_{GS} = 0.20$ V (subthreshold), $V_{GS} = 0.65$ V (max g_m), and $V_{GS} = 1.00$ V (saturation) for different pH solutions. In all pH sensing experiments and transfer characterization, V_{DS} was fixed at 0.7 V in the saturation region of the drain voltage.

Results and discussion

Fabrication of In_2O_3 NR FETs, influence of nanoribbon thickness on device performance, and structural uniformity characterization

In the first part of this work, we designed and optimized a wafer-scale process for the fabrication of highly uniform In_2O_3 NR FET devices with excellent electrical performance. Fig. 2a shows a photographic picture of a 4-inch SiO_2/Si wafer containing 22 In_2O_3 NR FET chips. Each chip has 4 independent NRs with corresponding on-chip integrated Au gate electrodes allowing multiplex sensing and assay control. SEM imaging of the fabricated NRs confirmed that smooth and straight In_2O_3 NRs (W:L: 3.7 × 14.0 μm) with source (S) and drain (D) metal electrodes were reliably fabricated throughout the whole 4-inch wafer using an optimized image reversal process (Fig. 2b). This

Open Access Article. Published on 05 November 2019. Downloaded on 1/24/2026 9:40:33 AM.
This article is licensed under a Creative Commons Attribution-NonCommercial 3.0 Unported Licence.

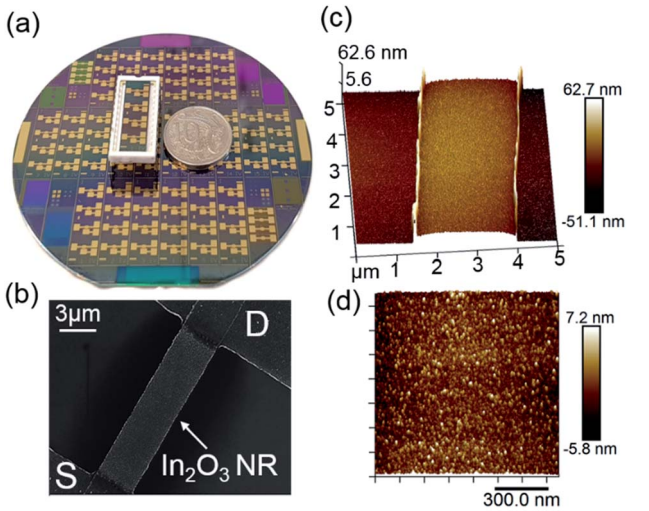

Fig. 2 (a) Photograph of a 4-inch SiO_2/Si wafer with 22 In_2O_3 NR FETs. On top of the wafer is a DIP packaged chip; (b) SEM image of In_2O_3 NR FETs with source and drain metal electrodes; (c) AFM cross-sectional image of a 30 nm In_2O_3 NR on Si substrate; (d) roughness characterization of the fabricated In_2O_3 NR (rms: 1.75 nm).

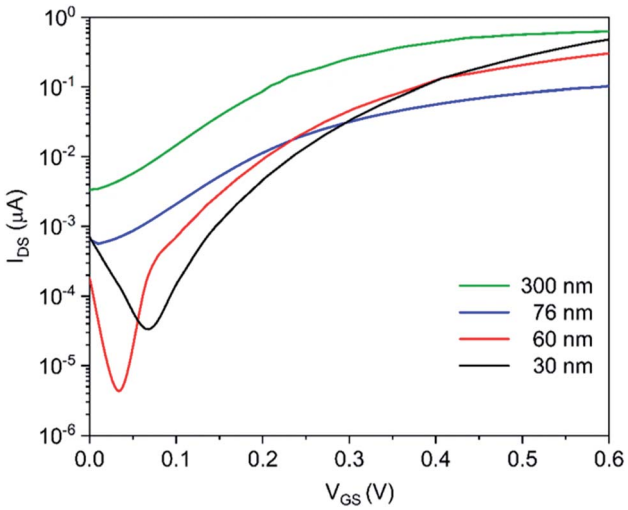

Fig. 3 Transfer curves of In_2O_3 NR FETs *versus* thicknesses.

process can be used to reliably define features down to 0.5 μm with high uniformity across the whole wafer. The RF sputtering deposition rate for In_2O_3 was optimized at the rate of 2.0 nm min^{-1}, which yielded fine control over the NRs' thicknesses. As can be seen from the cross section image of a 30 nm In_2O_3 NR presented in Fig. 2c and d, low surface roughness (rms ~ 1.75 nm) was obtained. Such smooth surface at the nanoscale is an important factor to achieve high FET performance as discussed in the next section.

In order to investigate the influence of the In_2O_3 FET thickness on their performance, we fabricated nanoribbons with thicknesses of 15, 60, 76, and 300 nm. The 15 nm NRs exhibited significant performance variations and low fabrication yield due to electrical contact issues to the thin film and scattering effects at such low thicknesses. For devices with thicknesses from 30 nm and upward, as the thickness of In_2O_3 thin film increased, subthreshold swing values increased accordingly. Specifically, subthreshold swing values increased from 80 ± 6.8 mV per decade for 30 nm devices to 88 ± 9.1 mV per decade for 60 nm devices, 121 ± 17.1 for 76 nm devices, and 140 ± 10.2 mV per decade for 300 nm devices. Representative transfer curves are shown in Fig. 3. The curves show steeper slopes in the subthreshold regime for the thinner devices. Compared to the 60, 76, and 300 nm devices, the 30 nm devices had the steepest transfer curves in the subthreshold regime and therefore the smallest SS values which can be extrapolated to the highest sensitivities. This observation is consistent with a recent report on the effect on the subthreshold swings of shrinking nanowire widths.[8] It is worth to note that the SS value changes are non-linear *vs.* changes in sensors' thicknesses, which is typical for non-annealed amorphous metal-oxide semiconductor materials sensor. We selected 30 nm thick In_2O_3 films as this thickness provided the best combination between sensor performance and fabrication uniformity. Results and discussion hereafter are for 30 nm In_2O_3 nanoribbon devices.

The overarching goal of this work is to carry out a holistic investigation of the fabrication and operation of In_2O_3 NR FETs towards accelerating the translation of this technology into real-life applications. To this end, a quality control protocol throughout the entire fabrication process has been established to ensure high structural uniformities and material purity of the fabricated NRs. As can be seen in Fig. 4a, excellent uniformity of the patterned NRs widths is demonstrated with an average lateral dimension distribution of 3.68 ± 0.08 μm, measured from 260 NRs from 3 different batches. The wafer-scale thickness uniformity of the In_2O_3 NRs is also a critical factor that needs to be assessed. As shown in Fig. 4b, thickness mapping of the In_2O_3 sputtered on a 4-inch wafer indicated that an excellent homogeneity is achieved with a mean thickness of 28.57 nm. This translates to a degree of uniformity of 97.33%, which is better than the typical thickness uniformity of sputtered metal oxides.[36]

Aside from sensor's structural uniformity, a consistent chemical composition of the indium oxide among fabrication batches needs to be achieved. As shown in Fig. 4c, consistent indium percentages were demonstrated with a mean indium composition of 21.1 ± 0.5%, measured from elemental indium percentage of the deposited thin films from 7 different fabrication batches. Altogether, these results confirmed that this process allows for the reproducible, cost-effective and high yield fabrication of In_2O_3 NR FETs and is compatible with up-scale manufacturing of this sensing technology.

Electrical characteristics of the In_2O_3 NR FETs

Next, the electrical performance of the fabricated In_2O_3 NR FETs was characterized. Fig. 5a presents the output characteristic of a device obtained by scanning the source-drain voltage, V_{DS}, from 0.0 to 1.0 V while stepping the gate voltage, V_{GS}, from 0 to 0.4 V (0.08 V steps) using the on-chip gate electrode. Obvious increase of the I_{DS} in response to positive V_{GS} within both linear

Open Access Article. Published on 05 November 2019. Downloaded on 1/24/2026 9:40:33 AM.
This article is licensed under a Creative Commons Attribution-NonCommercial 3.0 Unported Licence.

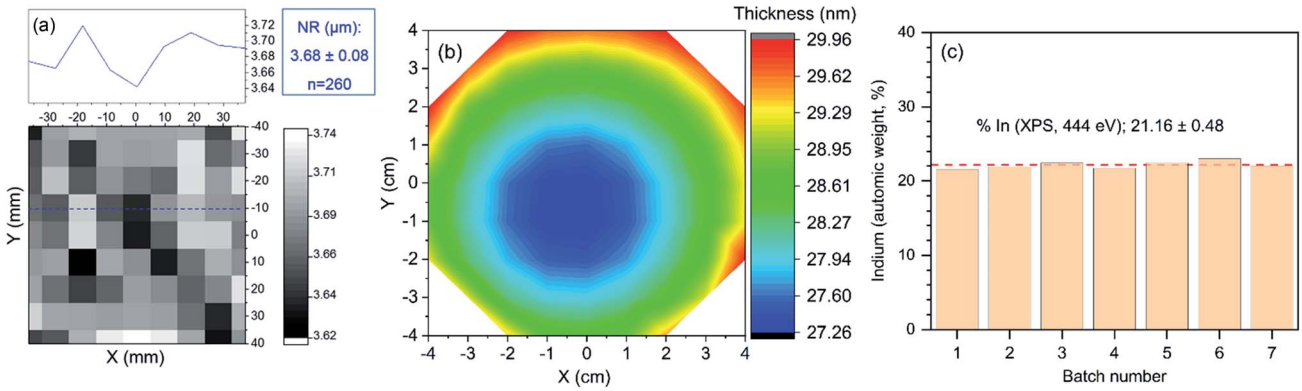

Fig. 4 (a) Measurement profile of 260 NRs width fabricated from 3 different batches; (b) ellipsometric thickness mapping of In_2O_3 deposited on a 4 inch wafer; (c) XPS percentage of indium from 7 fabrication batches.

and saturation regions was obtained, which is typical of a n-type enhancement long channel FET.[24,25,30,37] The transfer characteristic and subthreshold parameters of the device are also presented in Fig. 5b and c, respectively. Minor kinks are also observed in the drain current presented in Fig. 5a and b. The presence of such kink effect is a typical phenomenon in direct current FET measurement, which is attributed to impact ionization and electron capture and emission at deep levels.[38–41] From these graphs, the threshold voltage (V_{th}) of the devices were determined to be $V_{GS} = 0.35 \pm 0.03$ V. This low threshold voltage makes these In_2O_3 NR FETs devices suitable for applications requiring low power consumption such as wearable and battery powered point of care sensing. The devices' maximum transconductance $g_{m,max}$ was determined to be 3.93 ± 0.78 μS ($n = 57$). The devices' average field effect mobility was estimated to be 0.70 ± 0.14 cm^2 V^{-1} s^{-1} using the following equation:[23]

$$g_m = \frac{dI_{DS}}{dV_{GS}} = \frac{W}{L} C_{DL} \mu V_{DS} \quad (1)$$

where g_m is maximum transconductance of the devices obtained at V_{DS} of 0.7 V, W is the channel width (3.7 μm), L is the channel length (14.0 μm), and C_{DL} is the of electrical double layer capacitance per unit area in 1× PBS solution (30.12 μF cm^{-2}) as reported previously.[42]

On/off current ratio was determined to be 10^4 to 10^5, which is typical for un-annealed, amorphous In_2O_3 NR FETs.[10] Graphs presenting the statistical analyses of the 57 devices' threshold voltage, transconductance, field effect mobility and drain current on/off ratio are provided in the ESI (Fig. S3†).The leakage current was less than 5×10^{-10} A at $V_{GS} < 1.5$ V (Fig. S1, ESI†), which is compatible with liquid measurement in biochemical applications.

We then investigated the subthreshold swing, a key electrical property that reflects the FET device's performance.[43] As shown in Fig. 5b, the SS of the In_2O_3 NR FET device was determined to be 80 mV per decade, which is close to the limit of 60 mV per decade of the conventional MOSFETs[44,45] and is the highest performance when compared to previously reported values for nanoribbon based In_2O_3 FETs (Table 1). The low SS value achieved for In_2O_3 NR FETs is attributed to the systematically optimized fabrication process that allows the deposition of ultra-low surface roughness indium oxide thin film with uniform composition and dimensions[46,47] as well as the on-chip integration of the gate electrode.[48] In particular, previous studies have shown that the surface roughness has a major impact on the performance of nanoscale transistors. This is particularly important when scaling down the thicknesses of nanoribbon FETs. Due to surface/interface trapping and

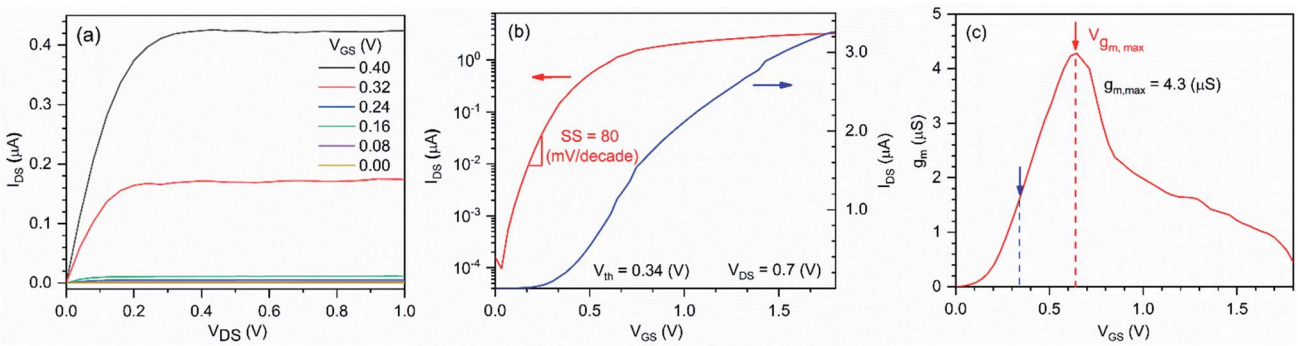

Fig. 5 (a) Output, (b) transfer characteristics, and (c) transconductance curve of the fabricated In_2O_3 NR FETs.

Open Access Article. Published on 05 November 2019. Downloaded on 1/24/2026 9:40:33 AM.
This article is licensed under a Creative Commons Attribution-NonCommercial 3.0 Unported Licence.

Table 1 Subthreshold swings for previously reported In_2O_3 NR FETs

Fabrication route	In_2O_3 dimensions (W:L:H, μm)	SS (mV per decade)	Ref.
Sol–gel synthesis	1 × 0.3 × 0.004	300	24
Inkjet printing	50 × 18 × not reported	180	49
Sol–gel	70 × 3000 × 0.010	1800	50
RF sputtering	150 × 2000 × 0.008	250	51
PECVD	200 × 200 × 0.100	500	52
ALD	20 × 40 × 0.005	90	53
RF sputtering	25 × 500 × 0.016	300	9
RF sputtering	3.7 × 14 × 0.030	80	This work

phonon-scattering, smooth sensor surfaces are indeed desirable toward achieving high performance FET signals.[46,47]

Mitigating device-to-device signal variation in the subthreshold regime

It is well established that in the subthreshold regime I_{DS} increases exponentially with V_{GS}, while I_{DS} only increases linearly in the linear regime. However, this intrinsic electronic differences between these two operation modes has never been exploited to reduce the device-to-device signal variations resulting from different batches. After batch-fabricating highly uniform In_2O_3 NR FETs, we systematically investigated the most appropriate operating bias focusing on improving the devices signal uniformity by analysing the electrical properties of 57 In_2O_3 NR FETs randomly selected from 3 independent different wafer-scale batches. Fig. 6a shows the plot of the mean I_{DS} (the dots) *versus* applied V_{GS} with the 95% confidence intervals (CI, the whiskers) and their respective standard deviation (SD) for each of the 57 devices. From the data, it can be seen that increasing applied V_{GS}, measured I_{DS} are more spread out, as shown from the larger confidence intervals and the increasing SD of I_{DS}. However, the magnitude of device-to-device I_{DS} variations in the subthreshold regime is comparatively lower than that measured in the linear regime. This is attributed to the intrinsic scattering of charge carriers (*i.e.* oxygen vacancies) within the In_2O_3 FET channels. When measured in a controlled environment (*e.g.* in a Faraday box), the variation of I_{DS} depends on two major factors: (1) the intrinsic device electrical properties of the channel (charge carrier density, carrier mobility, variations in structural dimensions); (2) the electric field exerted on the semiconductor channel caused by the applied V_{GS}. In our measurement, V_{GS} was applied through large on-chip electrode (W × L: 1800 × 1400 μm, Fig. S2 in ESI†) immersed in high ionic strength electrolyte 1× PBS (~15.5 mS cm^{-1}) for high measurement stability. Owing to the fact that the total number of charge carriers in each thin film device is not identical as well as owing to the presence of small structural differences, increased applied V_{GS} is expected to amplify the device-to-device differences leading in turn to larger signal variation. On the other hand, lower V_{GS} (below V_{th}) only affects a portion of the charge carriers inside the In_2O_3 NRs, which in turn results in lower device's conductivity but also lower devices' signal variation.

In order to determine the optimal operational condition for reducing device-to-device signal variation, we evaluated the relative changes in I/I_0 resolution when the devices are under the same magnitude of device surface potential change in the subthreshold and linear regimes. In both regimes, the normalization point, I_0, was chosen as the drain current at the lowest V_{GS} of each regime ($I_0 = I_{DS}$ at $V_{GS} = 0.17$ V for subthreshold and $I_0 = I_{DS}$ at $V_{GS} = 0.31$ V for the linear regime; detail for the I_{DS} normalization is shown in Fig. S4 in the ESI†). When drain currents at the highest V_{GS} of each regime are chosen as the normalization points, distributions of I/I_0 values

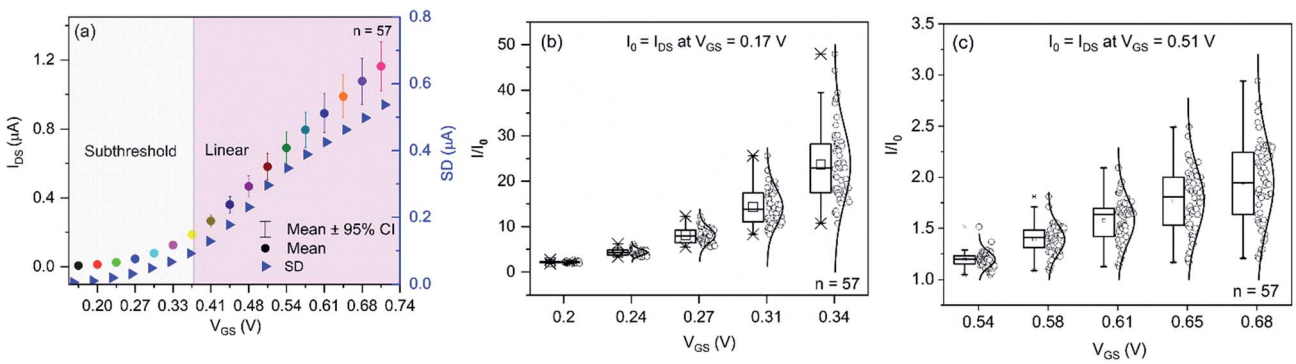

Fig. 6 (a) Drain currents (mean values with corresponding at 95% confidence level) *versus* applied gate voltages in the subthreshold and linear regimes for 57 In_2O_3 NR FETs; (b) distributions of I/I_0 of 57 In_2O_3 NR FETs in subthreshold ($I_0 = I_{DS}$ at $V_{GS} = 0.17$ V); and (c) in the linear regime ($I_0 = I_{DS}$ at $V_{GS} = 0.51$ V).

Open Access Article. Published on 05 November 2019. Downloaded on 1/24/2026 9:40:33 AM.
This article is licensed under a Creative Commons Attribution-NonCommercial 3.0 Unported Licence.

with respect to V_{GS} in the subthreshold and linear regimes showed the same trends with more dispersed data points in the linear regime compared with the subthreshold regime (Fig. S4†). The only differences are: (1) the magnitude of I/I_0 changes are now inversed to the changes when the lowest I_{DS} are chosen as normalization points. In particular, in the subthreshold regime, on average I_{DS} decreased 23.6 times from $V_{GS} = 0.34$ V to $V_{GS} = 0.17$ V when using the highest I_{DS} as normalization point (on average I_{DS} at $V_{GS} = 0.51$ V was 0.042). On the other hand, an average increase of 23.6 times for I_{DS} from $V_{GS} = 0.17$ V to $V_{GS} = 0.34$ V is obtained when using the lowest I_{DS} as normalization point. In the linear regime, I_{DS} increased/decreased only 2.1 times over the range of $V_{GS} = 0.68$ V to $V_{GS} = 0.51$ V. Because of the much bigger drain current changes over the range in the subthreshold regime, normalizing against the highest I_{DS} compresses the data points in the lower V_{GS} range as illustrated in the difference between Fig. 6b and S4a.† For better presentation of the data, we recommend normalizing against the lowest I_{DS}.

Next, we proceed to determine the optimal biasing point where the NR FET devices have the highest uniformity. By characterizing electrical signals from devices of different batches, we found out that there are two combining factors that significantly suppress device-to-device signal variation in the subthreshold regime while exacerbating the issue in the linear regime (Fig. 6b and c). In the subthreshold regime, I_{DS} increases much faster with V_{GS} change as compared with in the linear regime. For instance, I/I_0 exponentially increased an average of 22.5 times in the subthreshold regime while in the linear regime it just linearly increased by 2.1 times under the same measurement condition. At the same time, the magnitude of I_{DS} variation in the subthreshold is lower (sub-nA to nA) than that in the linear regime (sub-μA to μA). Therefore, data distributions from the 57 devices at each V_{GS} was better separated in the subthreshold regime as opposed to much poorer data distribution separation in the linear regime. For quantitative evaluation of data distribution separation, we calculated the quantitative resolutions (QR) of the signals using the formula:[54]

$$QR = \varepsilon_r/S \quad (2)$$

In which ε_r and S are the uncertainty of the measured response (variations from the 57 devices) and sensitivity (slope of calibration curve), respectively. Calibration curves for I/I_0 *versus* V_{GS} are provided in Fig. S5, ESI.† QR is a useful figure of merit to compare device performance in different regimes as it takes into account the variability of sensitivity and the uncertainty of the measured responses.[54] The smaller the QR value, the better resolved the signals. Calculated QRs for the subthreshold regime ranged from 0.009 to 0.019 V while QRs in the linear regime ranged from 0.02 to 0.08 V. The data showed that In_2O_3 NR FETs operated within the subthreshold regime could resolve I/I_0 signal change induced by as little as $V_{GS} = 9$ mV with respect to the device-to-device variation. On the other hand, at least 20 mV change in V_{GS} is required for the FETs operated in the linear regime. Due to the exponential change in the I_{DS} with V_{GS} in combination with lower magnitude of device-to-device signal variation, QRs in the subthreshold regime are at least 2 times higher than those in the linear regime. For the fabricated In_2O_3 NR FETs, the optimal operation point was determined to be $V_{GS} = 0.15$–0.2 V to achieve the best signal resolution.

Non-linear pH sensing with In_2O_3 NR FET

Next, the pH sensing performance of the In_2O_3 NR FETs was investigated from pH 10.4 to 4.0. As seen in Fig. 7, the sensors displayed more sensitive responses toward pH changes in the acidic (pH 4.0 to 7.0) compared to the basic (pH 7.0 to 10.0) pH ranges. Such non-linear pH response for the In_2O_3 FET can be explained by the site binding model.[55] Briefly, the In_2O_3 NRs' surface in contact with aqueous solution can hydrogenate to form hydroxide groups (–OH groups). These groups can either protonate or deprotonate leading to changes in the surface potential of the FET. In_2O_3 is an inorganic amphoteric oxide with a point-of-zero charge (PZC) of approximately 9.0.[56,57] This PZC results in higher pH sensitivity of the In_2O_3 devices in the acidic region and lower sensitivity in the more basic pH range

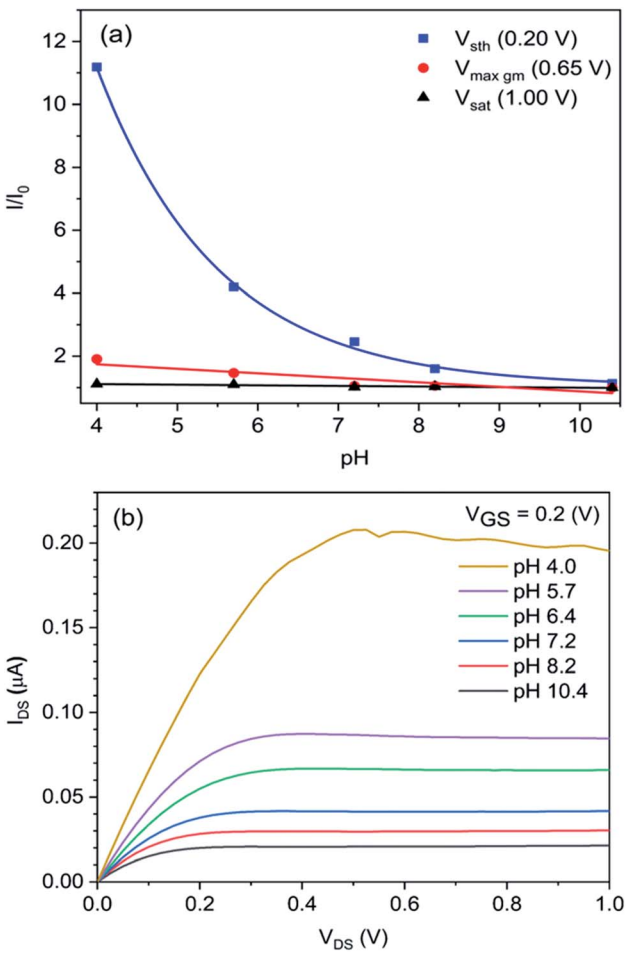

Fig. 7 (a) pH sensing of the developed In_2O_3 NR FETs in different V_{GS} regimes: subthreshold ($V_{GS} = 0.20$ V), maximum transconductance ($V_{GS} = 0.65$ V), and saturation ($V_{GS} = 0.10$ V), $V_{DS} = 0.7$ V; (b) absolute drain currents of the device with different pH values, $V_{GS} = 0.20$ V.

Open Access Article. Published on 05 November 2019. Downloaded on 1/24/2026 9:40:33 AM.
This article is licensed under a Creative Commons Attribution-NonCommercial 3.0 Unported Licence.

close to the PZC because of the differences in the magnitude of surface gating caused by the changes in pH. The exponential response to pH changes in the subthreshold regime and linear response in the linear regime are attributed to the well-known exponential and linear dependences of I_{DS} with V_{GS} in these regimes respectively as shown experimentally in Fig. 5b and mathematically in device physics.[58,59] In the saturation regime, no response to pH solution was observed as expected. An example of absolute drain current changes with pH solution is provided in Fig. 7b.

Conclusions

We report in this work a high performance In_2O_3 NR FET sensing platform. A steep subthreshold swing of 80 mV per decade was achieved through a combination of high quality In_2O_3 nanoribbon fabrication, stringent quality assessment as well as the implementation of an inbuilt gate electrode with a suitable device passivation layer. We systematically characterized and analysed the electrical properties of 57 In_2O_3 NR FETs from 3 different batches to reveal that device-to-device signal variation is significantly suppressed when the devices are operated in the subthreshold regime. This finding could serve as a useful operational reference for real-life sensing applications of nano FET sensors where sensing with multiple devices are required. Finally, a non-linear pH sensing response has been demonstrated on the fabricated devices. Combined with the availability of scalable and optimized fabrication processes, selecting the most appropriate operation conditions will foster the implementation of In_2O_3 NR FET devices in bioanalytical applications.

Conflicts of interest

There are no conflicts to declare.

Acknowledgements

This work is supported by the ARC Centre of Excellence in Convergent Bio-Nano Science and Technology and the DP170100170. Thuy Thi Thanh Pham acknowledges financial supports from Australia Awards Scholarships. D. P. Tran acknowledges the support of a Partnership Grant from UniSA. This work was performed in part at the South Australian and New South Wales node of the Australian National Fabrication Facility. The authors also would like to thank ANFF-SA node for their support.

References

1 D. Tran, T. Pham, B. Wolfrum, A. Offenhäusser and B. Thierry, *Materials*, 2018, **11**, 785.
2 G.-J. Zhang and Y. Ning, *Anal. Chim. Acta*, 2012, **749**, 1–15.
3 K.-I. Chen, B.-R. Li and Y.-T. Chen, *Nano Today*, 2011, **6**, 131–154.
4 M. O. Noor and U. J. Krull, *Anal. Chim. Acta*, 2014, **825**, 1–25.
5 F. Patolsky, G. Zheng and C. M. Lieber, *Nat. Protoc.*, 2006, **1**, 1711–1724.
6 D. P. Tran, M. A. Winter, B. Wolfrum, R. Stockmann, C.-T. Yang, M. Pourhassan-Moghaddam, A. Offenhäusser and B. Thierry, *ACS Nano*, 2016, **10**, 2357–2364.
7 N. Lu, A. Gao, P. Dai, S. Song, C. Fan, Y. Wang and T. Li, *Small*, 2014, **10**, 2022–2028.
8 K. Shoorideh and C. O. Chui, *Proc. Natl. Acad. Sci. U. S. A.*, 2014, **111**, 5111–5116.
9 Q. Liu, N. Aroonyadet, Y. Song, X. Wang, X. Cao, Y. Liu, S. Cong, F. Wu, M. E. Thompson and C. Zhou, *ACS Nano*, 2016, **10**, 10117–10125.
10 N. Aroonyadet, X. Wang, Y. Song, H. Chen, R. J. Cote, M. E. Thompson, R. H. Datar and C. Zhou, *Nano Lett.*, 2015, **15**, 1943–1951.
11 H.-K. Chang, F. N. Ishikawa, R. Zhang, R. Datar, R. J. Cote, M. E. Thompson and C. Zhou, *ACS Nano*, 2011, **5**, 9883–9891.
12 M. Curreli, C. Li, Y. Sun, B. Lei, M. A. Gundersen, M. E. Thompson and C. Zhou, *J. Am. Chem. Soc.*, 2005, **127**, 6922–6923.
13 A. L. D. Moreau, R. Janissen, C. A. Santos, L. A. Peroni, D. R. Stach-Machado, A. A. de Souza, A. P. de Souza and M. A. Cotta, *Biosens. Bioelectron.*, 2012, **36**, 62–68.
14 S. Upadhyay, R. Frederiksen, N. Lloret, L. D. Vico, P. Krogstrup, J. H. Jensen, K. L. Martinez and J. Nygård, *Appl. Phys. Lett.*, 2014, **104**, 203504.
15 R. Janissen, P. K. Sahoo, C. A. Santos, A. M. da Silva, A. A. G. von Zuben, D. E. P. Souto, A. D. T. Costa, P. Celedon, N. I. T. Zanchin, D. B. Almeida, D. S. Oliveira, L. T. Kubota, C. L. Cesar, A. P. d. Souza and M. A. Cotta, *Nano Lett.*, 2017, **17**, 5938–5949.
16 C. Li, M. Curreli, H. Lin, B. Lei, F. N. Ishikawa, R. Datar, R. J. Cote, M. E. Thompson and C. Zhou, *J. Am. Chem. Soc.*, 2005, **127**, 12484–12485.
17 S. Liu and X. Guo, *NPG Asia Mater.*, 2012, **4**, e23.
18 M. L. Hammock, O. Knopfmacher, T. N. Ng, J. B. Tok and Z. Bao, *Adv. Mater.*, 2014, **26**, 6138–6144.
19 V. Krivitsky, L.-C. Hsiung, A. Lichtenstein, B. Brudnik, R. Kantaev, R. Elnathan, A. Pevzner, A. Khatchtourints and F. Patolsky, *Nano Lett.*, 2012, **12**, 4748–4756.
20 O. Knopfmacher, A. Tarasov, W. Fu, M. Wipf, B. Niesen, M. Calame and C. Schönenberger, *Nano Lett.*, 2010, **10**, 2268–2274.
21 G. S. Kulkarni and Z. Zhong, *Nano Lett.*, 2012, **12**, 719–723.
22 P. E. Sheehan and L. J. Whitman, *Nano Lett.*, 2005, **5**, 803–807.
23 Q. Liu, Y. Liu, F. Wu, X. Cao, Z. Li, M. Alharbi, A. N. Abbas, M. R. Amer and C. Zhou, *ACS Nano*, 2018, **12**, 1170–1178.
24 J. Kim, Y. S. Rim, H. Chen, H. H. Cao, N. Nakatsuka, H. L. Hinton, C. Zhao, A. M. Andrews, Y. Yang and P. S. Weiss, *ACS Nano*, 2015, **9**, 4572–4582.
25 C. Li, B. Lei, D. Zhang, X. Liu, S. Han, T. Tang, M. Rouhanizadeh, T. Hsiai and C. Zhou, *Appl. Phys. Lett.*, 2003, **83**, 4014–4016.
26 X. Zou, X. Liu, C. Wang, Y. Jiang, Y. Wang, X. Xiao, J. C. Ho, J. Li, C. Jiang, Q. Xiong and L. Liao, *ACS Nano*, 2013, **7**, 804–810.

Open Access Article. Published on 05 November 2019. Downloaded on 1/24/2026 9:40:33 AM.
This article is licensed under a Creative Commons Attribution-NonCommercial 3.0 Unported Licence.

27 D. Zhang, Z. Liu, C. Li, T. Tang, X. Liu, S. Han, B. Lei and C. Zhou, *Nano Lett.*, 2004, **4**, 1919–1924.
28 W. J. Maeng, D.-w. Choi, K.-B. Chung, W. Koh, G.-Y. Kim, S.-Y. Choi and J.-S. Park, *ACS Appl. Mater. Interfaces*, 2014, **6**, 17481–17488.
29 J. Sheng, D.-w. Choi, S.-H. Lee, J. Park and J.-S. Park, *J. Mater. Chem. C*, 2016, **4**, 7571–7576.
30 J. H. Noh, S. Y. Ryu, S. J. Jo, C. S. Kim, S. W. Sohn, P. D. Rack, D. J. Kim and H. K. Baik, *IEEE Electron Device Lett.*, 2010, **31**, 567–569.
31 Z. Yuan, X. Zhu, X. Wang, X. Cai, B. Zhang, D. Qiu and H. Wu, *Thin Solid Films*, 2011, **519**, 3254–3258.
32 S. K. Garlapati, T. T. Baby, S. Dehm, M. Hammad, V. S. K. Chakravadhanula, R. Kruk, H. Hahn and S. Dasgupta, *Small*, 2015, **11**, 3591–3596.
33 F. N. Ishikawa, M. Curreli, H.-K. Chang, P.-C. Chen, R. Zhang, R. J. Cote, M. E. Thompson and C. Zhou, *ACS Nano*, 2009, **3**, 3969–3976.
34 M. O. Hill, I. Calvo-Almazan, M. Allain, M. V. Holt, A. Ulvestad, J. Treu, G. Koblmüller, C. Huang, X. Huang, H. Yan, E. Nazaretski, Y. S. Chu, G. B. Stephenson, V. Chamard, L. J. Lauhon and S. O. Hruszkewycz, *Nano Lett.*, 2018, **18**, 811–819.
35 S. Labat, M.-I. Richard, M. Dupraz, M. Gailhanou, G. Beutier, M. Verdier, F. Mastropietro, T. W. Cornelius, T. U. Schülli, J. Eymery and O. Thomas, *ACS Nano*, 2015, **9**, 9210–9216.
36 M. Matsuoka and S. i. Tohno, *J. Vac. Sci. Technol., A*, 1995, **13**, 2427–2434.
37 C.-H. Choi, S.-Y. Han, Y.-W. Su, Z. Fang, L.-Y. Lin, C.-C. Cheng and C.-h. Chang, *J. Mater. Chem. C*, 2015, **3**, 854–860.
38 J. Haruyama, H. Negishi, Y. Nishimura and Y. Nashimoto, *IEEE Trans. Electron Devices*, 1997, **44**, 25–33.
39 J. Haruyama, Y. Ohno, H. Katano and Y. Nashimoto, *IEEE Trans. Electron Devices*, 1994, **41**, 1873–1875.
40 K. Kato, T. Wada and K. Taniguchi, *IEEE Trans. Electron Devices*, 1985, **32**, 458–462.
41 M. Narayanan, H. Al-Nashash, B. Mazhari, D. Pal and M. Chandra, *Act. Passive Electron. Compon.*, 2012, **2012**, 1–9.
42 S. Park, S. Lee, C.-H. Kim, I. Lee, W.-J. Lee, S. Kim, B.-G. Lee, J.-H. Jang and M.-H. Yoon, *Sci. Rep.*, 2015, **5**, 13088.
43 W. Cao, D. Sarkar, Y. Khatami, J. Kang and K. Banerjee, *AIP Adv.*, 2014, **4**, 067141.
44 Q. Xu, X. Liu, B. Wan, Z. Yang, F. Li, J. Lu, G. Hu, C. Pan and Z. L. Wang, *ACS Nano*, 2018, **12**, 9608–9616.
45 Z. Qin, Z. Wei and A. Seabaugh, *IEEE Electron Device Lett.*, 2006, **27**, 297–300.
46 F. Wang, S. Yip, N. Han, K. Fok, H. Lin, J. J. Hou, G. Dong, T. Hung, K. S. Chan and J. C. Ho, *Nanotechnology*, 2013, **24**, 375202.
47 D. P. Tran, B. Wolfrum, R. Stockmann, A. Offenhäusser and B. Thierry, *J. Mater. Chem. C*, 2014, **2**, 5229–5234.
48 H. J. N. P. D. Mello, S. Dalgleish, G. Ligorio, M. Mulato and E. J. W. List-Kratochvil, Organic and Hybrid Sensors and Bioelectronics XI, *SPIE Proceedings*, 2018, vol. 10738, p. 1073819.
49 H. Basem, L. You, Y. Jason, Y. Yang, G. Kumaravelu, W. Andrew, E. Robin, C. Gursharan, N. Babak and S. Efstratios, *Flexible Printed Electron.*, 2018, **3**, 042001.
50 C. Kookhyun, K. Minseok, C. Seongpil, O. Tae-Yeon, J. Shin Woo, H. Hyeon Jun and J. Byeong-Kwon, *Jpn. J. Appl. Phys.*, 2013, **52**, 060204.
51 J. H. Noh, S. Y. Ryu, S. J. Jo, C. S. Kim, S. Sohn, P. D. Rack, D. Kim and H. K. Baik, *IEEE Electron Device Lett.*, 2010, **31**, 567–569.
52 Y. Vygranenko, K. Wang and A. Nathan, *Appl. Phys. Lett.*, 2007, **91**, 263508.
53 H. I. Yeom, J. B. Ko, G. Mun and S. H. K. Park, *J. Mater. Chem. C*, 2016, **4**, 6873–6880.
54 H. L. Pardue, *Clin. Chem.*, 1997, **43**, 1831.
55 D. E. Yates, S. Levine and T. W. Healy, *J. Chem. Soc., Faraday Trans. 1*, 1974, **70**, 1807–1818.
56 J. A. R. M. Fernández-García, *Synthesis, Properties, and Applications of Oxide Nanomaterials*, John Wiley & Sons, Inc., Hoboken, NJ, USA, 2006, ch. 2, pp. 49–78, ISBN: 978-0-471-72405-6.
57 M. Kosmulski, *J. Colloid Interface Sci.*, 2001, **238**, 225–227.
58 W. Deng, X. Ma and J. Huang, *AIP Adv.*, 2014, **4**, 087107.
59 W. Deng and J. Huang, *IEEE Electron Device Lett.*, 2011, **32**, 647–649.